Optics Letters

Ultra-compact on-chip phonon-polaritonic mode converter

Jiayu Ye,[1] Runzhi Cao,[1] Chong Sheng,[1,*] Mingyuan Gao,[1] Yule Zhao,[1] Dawei Liu,[1] Yong Zhou,[1] Shining Zhu,[1] and Hui Liu[1,2]

[1]National Laboratory of Solid State Microstructures and School of Physics, Collaborative Innovation Center of Advanced Microstructures, Nanjing University, Nanjing, Jiangsu 210093, China
[2]liuhui@nju.edu.cn
*csheng@nju.edu.cn

Received 14 May 2025; revised 11 June 2025; accepted 17 June 2025; posted 18 June 2025; published 15 July 2025

On-chip optical interconnects promise unprecedented manipulation of information processing with the advantages of a large bandwidth, low energy consumption, and anti-interference capability. Among the key components of optical interconnects, the mode converter plays an irreplaceable role. Currently, conventional mode converters face challenges such as insufficient compactness, limited integration, and functional singularity. Here, we propose an ultra-compact mode converter on a phonon-polaritonic chip. Specifically, we judiciously leverage the landmark hyperbolic dispersion of van der Waals crystals combined with the light manipulation capabilities of metasurfaces to realize high-efficiency mode conversion. The proposed converter can simultaneously achieve multimode conversion with high efficiency within a conversion length of only one working wavelength in free space, significantly enhancing compactness and functional versatility compared to previous designs. Our method establishes a new paradigm for developing highly integrated and ultra-thin nanophotonic devices on phonon-polaritonic chips.

https://doi.org/10.1364/OL.567551

Introduction. The contemporary information society has entered the era of big data, which puts forward ever-increasing demands for information processing systems. To deal with these challenges, integrated photonics that can transfer and process massive information has garnered substantial attention. Various material platforms of integrated photonics have been developed, ranging from silicon photonics and lithium niobate photonics to III–V semiconductor-based systems, and so on. Recently, the emergent polaritons in polar crystals, such as hexagonal boron nitride (hBN) and α-phase molybdenum trioxide (α-MoO_3), feature ultra-high confinement of electromagnetic waves into a deeply subwavelength scale, bringing promise for their use in integrated and ultra-thin nanophotonic devices. Remarkable examples of these phonon polaritons (PhPs) include sub-diffractional focusing and imaging [1–3], wavefront shaping [4–7] using metasurfaces and nanointerfaces, topological transition [8], and nanolight canalization [9,10], negative refraction [11], and reversed Cherenkov radiation [12], among others. Notably, these unique applications are mainly ascribed to their natural hyperbolic dispersion of polar crystals. The underlying reason lies in the unique hyperbolic dispersion characteristics: this phenomenon provides infinite wavevector momentum and exhibits strong optical anisotropy, enabling nanoscale light field manipulation. Such properties facilitate the generation of high-density photonic states and significantly enhance light–matter interactions, thereby offering transformative potential for designing next-generation integrated photonic devices. Despite these successes, the utilization of this unusual dispersion to realize a functional integrated photonic device on a phonon-polaritonic chip remains elusive.

At the same time, the multiplexing technologies developed for integrated photonic devices, such as wavelength division multiplexing, polarization division multiplexing, and mode division multiplexing (MDM), are assumed to efficiently increase the channel number and thus the information capacity. In MDM technology, mode converters are crucial for data transfer between channels. Various mode conversion strategies have been developed, each presenting distinct trade-offs: multimode interference couplers [13,14] exploit self-imaging phenomena but require extended conversion lengths. Adiabatic tapered waveguides [15,16] preserve mode orthogonality but sacrifice compactness due to their considerable footprint. Inverse-designed structures [17–19] achieve spatial compression through optimization algorithms, though their operational principles often lack physical transparency. Alternative approaches including anti-symmetric waveguide Bragg gratings [20], 2D photonic crystals [21,22], Y-junction waveguides [23,24], and asymmetric directional couplers [25,26] typically demand extended interaction regions (spanning multiple to hundreds of free-space wavelengths) to satisfy phase-matching conditions and facilitate modal interference. This inherent limitation underscores the critical need for developing next-generation ultra-compact solutions. Emerging metasurface platforms [27–30] offer transformative potential through subwavelength-scale architectures, enabling simultaneous enhancement of both device miniaturization and mode conversion efficiency. This raises a critical question: can the synergistic integration of intrinsic hyperbolic

dispersion, characterized by unbounded momentum states, and metasurface-enabled subwavelength light manipulation enable the development of ultra-compact mode converters, with device lengths approaching or even smaller than one working wavelength?

In this work, we propose an ultra-compact mode converter designed with a gradient meta-phonon-polaritons waveguide, whose structure consists of air/α-MoO_3/metasurfaces/SiO_2. Thanks to the intrinsic hyperbolic dispersion in α-MoO_3, we achieve highly efficient phonon-polariton mode conversion within a propagation length of just one working wavelength in free space. Additionally, unlike previous mode-converter devices, which are designed for specific waveguide modes, our proposed mode converter enables simultaneous multimode conversion with high efficiency.

Theory of dispersion of a structured waveguide. To achieve on-chip mode conversion for phonon polaritons, we exploit the intrinsic hyperbolic dispersion of α-MoO_3 by sandwiching it between two semi-infinite isotropic media (air and SiO_2), with dielectric permittivities ε_1 and ε_3, respectively, thereby forming a biaxial slab waveguide. The biaxial material α-MoO_3 has the dielectric tensor $\ddot{\varepsilon}_2 = \mathrm{diag}[\varepsilon_x, \varepsilon_y, \varepsilon_z]$ and exhibits three hyperbolic Reststrahlen bands (RBs) due to its anisotropic phonon responses: RB1 (545–851 cm^{-1}), RB2 (820–972 cm^{-1}), and RB3 (958–1004 cm^{-1}). These bands support hyperbolic phonon polaritons dominated by transverse magnetic (TM) modes, as the isofrequency contours of transverse electric (TE) modes form closed surfaces with finite wave vectors, whereas hyperbolic modes exhibit open surfaces with large wave vectors. Assuming in-plane propagation along the principal y-axis, the electric and magnetic fields are expressed as: $\vec{E}(z,y,t) = \vec{e}E(z)\exp(iqy - i\omega t)$ and $\vec{H}(z,y,t) = \vec{e}H(z)\exp(iqy - i\omega t)$, where the propagation constant is $q = n_{\mathrm{eff}}k_0$, with n_{eff} being the effective refractive index and k_0 being the vacuum wave vector. For TM modes (nonzero components: (E_y, H_x, E_z)), solving Maxwell's equations yields the dispersion relation [3]:

$$k_z d = \arctan\left(\frac{\alpha_1}{\varepsilon_1}\frac{\varepsilon_y}{k_z}\right) + \arctan\left(\frac{\alpha_3}{\varepsilon_3}\frac{\varepsilon_y}{k_z}\right) + m\pi, \qquad (1)$$

where $k_z = \sqrt{k_0^2\varepsilon_y - \frac{\varepsilon_y q^2}{\varepsilon_z}}$ and $\alpha_{1,3} = \sqrt{q^2 - k_0^2\varepsilon_{1,3}}$ represent the z-component of momenta in α-MoO_3, air, and SiO_2, respectively. d is the slab thickness, and $m = 0, 1, 2\ldots$ is the TM mode order.

Using Eq. (1), we calculate the dispersion for different RBs [31]. In RB1 and RB2, hyperbolic responses arise with $\mathrm{Re}(\varepsilon_y) < 0$, $\mathrm{Re}(\varepsilon_x) \neq \mathrm{Re}(\varepsilon_z) > 0$ and $\mathrm{Re}(\varepsilon_x) < 0$, $\mathrm{Re}(\varepsilon_y) \neq \mathrm{Re}(\varepsilon_z) > 0$. For RB2, the effective refractive index is bounded by $\varepsilon_3 < n_{eff} < \mathrm{Re}(\varepsilon_z)$. Since our focus is on highly confined polaritons with large n_{eff}, RB2 is excluded from further analysis. Figure 1(b) shows the TM mode dispersion at 674 cm^{-1} (RB1), while Fig. 1(c) displays the corresponding dispersion at 986 cm^{-1} (RB3), where $\mathrm{Re}(\varepsilon_z) < 0$, $\mathrm{Re}(\varepsilon_x) \neq \mathrm{Re}(\varepsilon_y) > 0$. Notably, unlike isotropic waveguides where n_{eff} increases with slab thickness (Fig. 1(d)), the biaxial slab exhibits an inverse trend: n_{eff} rises as slab thickness decreases. Furthermore, a critical thickness exists as a turning point for the fundamental mode in RB3 (Fig. 1(c)), beyond which this low-order TM modes vanish. This unique dispersion enables on-chip mode conversion, as discussed below with metasurface integration.

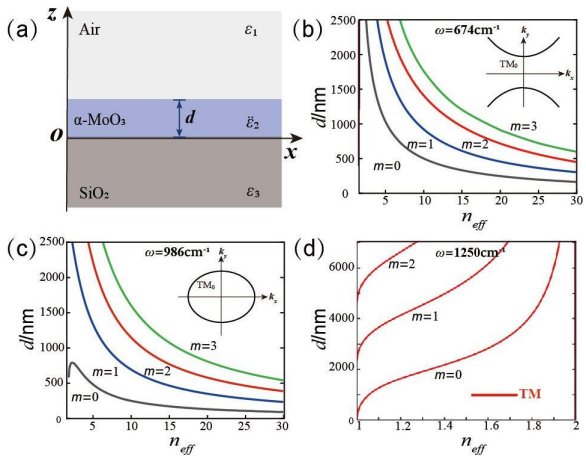

Fig. 1. α-MoO_3 slab waveguide and different TM mode dispersion. (a) Schematic of the waveguide model. Effective refractive index versus slab thickness at 674 cm^{-1} (b) and 986 cm^{-1} (c). (d) Conventional slab waveguide dispersion.

Mode conversion with the assistance of metasurface. To achieve adiabatic mode conversion within a single working wavelength, we leverage the intrinsic hyperbolic dispersion of α-MoO_3 in conjunction with metasurface to construct a meta-phonon-polaritonic waveguide. The metasurface parameters are: grating period ($p = 600$ nm), thickness ($t = 300$ nm), and α-MoO_3 filling ratio (f), where f is defined as α-MoO_3's filling width (w) divided by the grating period p: $f = w/p$. Using effective medium theory [32], the effective permittivities are: $\varepsilon_{\mathrm{eff},x} = 1/\left[\frac{f}{\varepsilon_x} + \frac{1-f}{\varepsilon_3}\right]$, $\varepsilon_{\mathrm{eff},y(z)} = f\varepsilon_{y(z)} + (1-f)\varepsilon_3$. The TM mode dispersion of this structure is:

$$k_z d = \arctan\left[\frac{-B\cdot\tan\left(k_{\mathrm{eff},z}t\right) + C}{A\cdot\tan\left(k_{\mathrm{eff},z}t\right) + D}\right] + m\pi, \qquad (2)$$

where $k_{\mathrm{eff},z} = \sqrt{k_0^2\varepsilon_{\mathrm{eff},y} - \frac{\varepsilon_{\mathrm{eff},y}q^2}{\varepsilon_{\mathrm{eff},z}}}$, and coefficients ($A$, B, C, D) are defined as: $A = \frac{k_z^2\varepsilon_{\mathrm{eff},y}\alpha_3}{k_{\mathrm{eff},z}\varepsilon_y^2\varepsilon_3} + \frac{k_{\mathrm{eff},z}\alpha_1}{\varepsilon_{\mathrm{eff},y}\varepsilon_1}$, $B = \frac{k_{\mathrm{eff},z}k_z}{\varepsilon_{\mathrm{eff},y}\varepsilon_y} - \frac{k_z\varepsilon_{\mathrm{eff},y}\alpha_1\alpha_3}{k_{\mathrm{eff},z}\varepsilon_y\varepsilon_1\varepsilon_3}$, $C = \frac{k_z}{\varepsilon_y}\left(\frac{\alpha_1}{\varepsilon_1} + \frac{\alpha_3}{\varepsilon_3}\right)$, and $D = \frac{k_z^2}{\varepsilon_y^2} - \frac{\alpha_1\alpha_3}{\varepsilon_1\varepsilon_3}$. Figure 2 shows the TM mode dispersion calculated via Eq. (2). Full-wave simulations (COMSOL Multiphysics) validate the analytical results. Notably, at 986 cm^{-1} frequency (RB3), the TM_0 mode gradually vanishes as the filling ratio (f) increases (Figs. 2(b)–2(e)) for a chosen slab thickness, whereas all modes persist at 674 cm^{-1} frequency (Figs. 2(f)–2(i)). This selective mode suppression in RB3 enables metasurface-assisted phonon-polariton mode conversion.

Next, we design a gradient meta-phonon-polariton waveguide with metasurfaces whose filling ratio adiabatically varies along the propagation direction (Fig. 3(a)). Using first-principles simulations (Lumerical FDTD), we analyze mode evolution as phonon polaritons propagate through the structure. At 986 cm^{-1} frequency, the TM_0 mode gradually converts to TM_1 mode in the forward direction (Fig. 3(b)). In contrast, no mode conversion occurs at 674 cm^{-1} frequency. Remarkably, near-perfect conversion efficiency is achieved within a 10-μm propagation length—approximately one free-space wavelength. To our knowledge, this represents unprecedented compactness compared to conventional mode converters. Additionally, the converter supports parallel multimode conversion: TM_1 (TM_2)

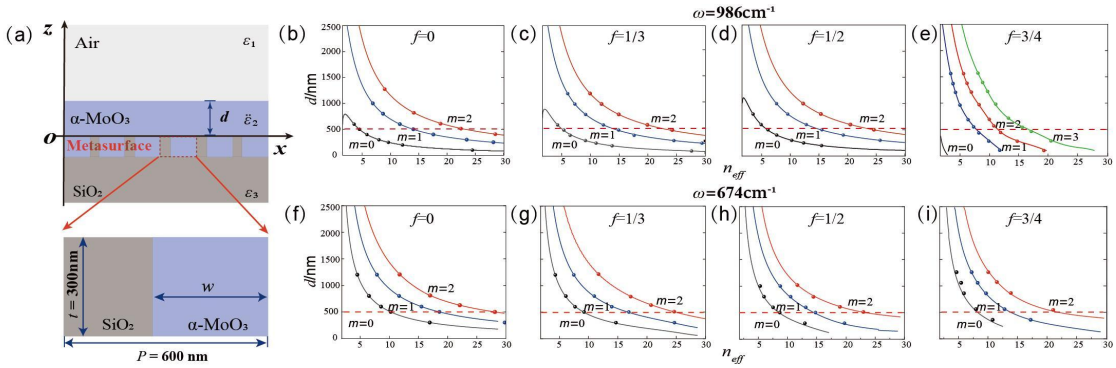

Fig. 2. Metasurface-embedded α-MoO_3 slab waveguide: (a) Schematic of the metasurface-waveguide model. Effective refractive index versus thickness at 986 cm^{-1} ((b)–(e)) and 674 cm^{-1} ((f)–(i)) in various filling ratios. The solid lines and dots are analytical (simulation) solutions. The red dashed lines indicate 500 nm thickness.

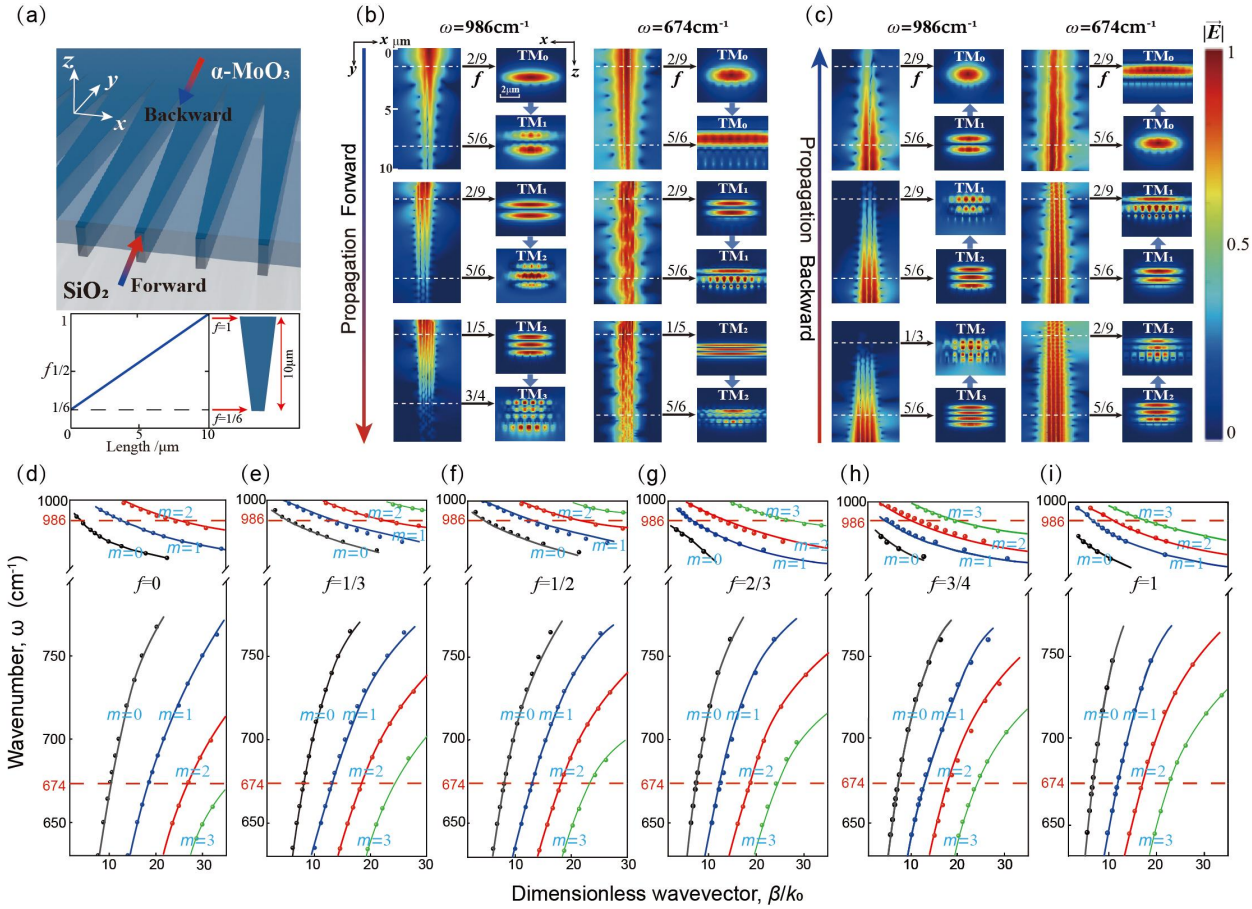

Fig. 3. Gradient meta-phonon-polaritonic waveguide. (a) Schematic of mode converter. (b), (c) Mode evolution in forward and backward propagations at 986 cm^{-1} and 674 cm^{-1}. (d)–(i) Evolution of dispersion relations with various filling ratios.

can similarly transform to TM_2 (TM_3) with high efficiency. Since time-reversal symmetry is preserved, backward propagation enables reverse conversion ($TM_3 \rightarrow TM_2$, $TM_2 \rightarrow TM_1$, and $TM_1 \rightarrow TM_0$) at 986 cm^{-1} frequency, as shown in Fig. 3(c). On the contrary, all modes still remain stable at 674 cm^{-1} frequency.

To elucidate the physics of mode conversion, we calculate the frequency-wavevector dispersion for the gradient meta-phonon-polariton waveguide with varying filling ratios. Since the gradient structure breaks translational symmetry but lacks nonlinear effects, the phonon-polariton frequency remains invariant during mode conversion. This invariance allows us to trace the conversion process on the dispersion diagram. Figures 3(d)–3(i) show that all mode dispersions shift downward with increasing filling ratio for phonon polaritons in RB3. This suggests that when the lowest-order mode is launched at a chosen frequency before entering the gradient meta-waveguide, the dispersion progressively ceases to support this mode due

to the increasing filling ratio, as shown in Fig. 3(g). As a result, it transitions to the nearest higher-order mode, as shown in Figs. 3(h) and 3(i). Simultaneously, all other higher-order modes transform to their respective next-higher orders. In contrast, for phonon polaritons in RB1, the dispersion profile remains stable, ensuring persistent maintenance of the waveguide mode throughout propagation in the gradient meta-waveguide. This analysis elucidates why multimode conversion occurs at 986 cm^{-1} frequency but is absent at 674 cm^{-1} frequency. Additionally, quantitative metrics of this mode converter have been compared in Supplement 1 (S.1 and S.2).

Conclusion. In this Letter, we have proposed an ultra-compact mode converter using metasurface on a phonon-polaritonic chip. We demonstrate the strategic utilization of α-MoO_3's intrinsic hyperbolic dispersion to achieve high-efficiency multimode conversion. To our knowledge, the proposed converter exhibits the shortest conversion length reported to date. This methodology can be extended to other hyperbolic biaxial van der Waals crystals, enabling the construction of on-chip mode-conversion devices. Although the concept is theoretical in design, it remains experimentally viable. For example, α-MoO_3 now benefits from well-established fabrication techniques, where high-quality α-MoO_3 layers can be synthesized via chemical vapor deposition (CVD) [33]. Additionally, metasurface patterning on two-dimensional materials has been successfully demonstrated using conventional micro/nanofabrication approaches [7,34]. These findings establish new paradigms for developing highly integrated, ultra-thin nanophotonic systems.

Funding. National Key Research and Development Program of China (2023YFB2805700); the National Natural Science Foundation of China (12174187, 62288101, 92163216, 92463308); the Natural Science Foundation of Jiangsu Province, China (BK20240164, BK20243009); and the Fundamental Research Funds for the Central Universities (2024300329).

Disclosures. The authors declare no conflicts of interest.

Data availability. Data underlying the results presented in this paper are not publicly available at this time but may be obtained from the authors upon reasonable request.

Supplemental document. See Supplement 1 for supporting content.

REFERENCES

1. S. Dai, Q. Ma, T. Andersen, *et al.*, Nat. Commun. **6**(1), 6963 (2015).
2. P. Li, M. Lewin, A. V. Kretinin, *et al.*, Nat. Commun. **6**(1), 7507 (2015).
3. S. Tao, T. Hou, Y. Zeng, *et al.*, Photonics Res. **10**(10), B14 (2022).
4. P. Li, I. Dolado, F. J. Alfaro-Mozaz, *et al.*, Science **359**(6378), 892 (2018).
5. K. Chaudhary, M. Tamagnone, X. Yin, *et al.*, Nat. Commun. **10**(1), 4487 (2019).
6. J. Duan, G. Álvarez-Pérez, A. I. F. Tresguerres-Mata, *et al.*, Nat. Commun. **12**(1), 4325 (2021).
7. W. Huang, T. Folland, F. Sun, *et al.*, Nat. Commun. **14**(1), 2716 (2023).
8. J. Duan, G. Álvarez-Pérez, K. V. Voronin, *et al.*, Sci. Adv. **7**(14), eabf2690 (2021).
9. G. Hu, Q. Ou, G. Si, *et al.*, Nature **582**(7811), 209 (2020).
10. P. Li, G. Hu, I. Dolado, *et al.*, Nat. Commun. **11**(1), 3663 (2020).
11. A. J. Sternbach, S. L. Moore, A. Rikhter, *et al.*, Science **379**(6632), 555 (2023).
12. X. Guo, C. Wu, S. Zhang, *et al.*, Nat. Commun. **14**(1), 2532 (2023).
13. J. Leuthold, J. Eckner, E. Gamper, *et al.*, J. Lightwave Technol. **16**(7), 1228 (1998).
14. S. Y. Tseng and M. Wu, IEEE Photonics Technol. Lett. **22**(16), 1211 (2010).
15. D. Dai and J. Bowers, Opt. Express **19**(11), 10940 (2011).
16. D. Dai, Y. Tang, and J. E. Bowers, Opt. Express **20**(12), 13425 (2012).
17. J. Lu and J. Vuckovic, Opt. Express **20**(7), 7221 (2012).
18. H. Zhou, K. Liao, Z. Su, *et al.*, Nanophotonics **12**(6), 1105 (2023).
19. Q. Ling, P. Dong, Y. Chu, *et al.*, Chip **2**(4), 100061 (2023).
20. J. Castro, D. F. Geraghty, S. Honkanen, *et al.*, Opt. Express **13**(11), 4180 (2005).
21. G. Chen and J. U. Kang, Opt. Lett. **30**(13), 1656 (2005).
22. V. Liu, D. A. B. Miller, and S. Fan, Opt. Express **20**(27), 28388 (2012).
23. Y. Huang, G. Xu, and S. Ho, IEEE Photonics Technol. Lett. **18**(21), 2281 (2006).
24. B. B. Oner, K. Ustun, H. Kurt, *et al.*, Opt. Express **23**(3), 3186 (2015).
25. Y. Ding, X. Ji, F. D. Ros, *et al.*, Opt. Express **21**(8), 10376 (2013).
26. Y. Yang, Y. Li, Y. Huang, *et al.*, Opt. Express **22**(18), 22172 (2014).
27. H. Qiu, H. Yu, T. Hu, *et al.*, Opt. Express **21**(15), 17904 (2013).
28. D. Ohana, B. Desiatov, N. Mazurski, *et al.*, Nano Lett. **16**(12), 7956 (2016).
29. Z. Li, M. H. Kim, C. Wang, *et al.*, Nat. Nanotechnol. **12**(7), 675 (2017).
30. X. Yi, C. Li, W. Zhao, *et al.*, Nanophotonics **12**(9), 1809 (2023).
31. Z. Zheng, N. Xu, S. Oscurato, *et al.*, Sci. Adv. **5**(5), eaav8690 (2019).
32. Z. Jacob and E. E. Narimanov, Appl. Phys. Lett. **93**(22), 221109 (2008).
33. S. Zhou, L. Gan, D. Wang, *et al.*, Nano Res. **11**(6), 2909 (2018).
34. A. Hohenau, H. Ditlbacher, B. Lamprecht, *et al.*, Microelectron. Eng. **83**(4–9), 1464 (2006).